IJE TRANSACTIONS B: Applications Vol. 33, No. 8, (August 2020) 1529-1543

International Journal of Engineering

Journal Homepage: www.ije.ir

Numerical and Experimental Investigations on the Behavior of Steel-reinforced Concrete Columns Subjected to Eccentric Loading

M. Ahmadi[a], M. Naghipour*[a], M. Nematzadeh[b]

[a] *Faculty of Civil Engineering, Babol Noshirvani University of Technology, Babol, Iran*
[b] *Department of Civil Engineering, University of Mazandaran, Babolsar, Iran*

PAPER INFO

Paper history:
Received 27 March 2020
Received in revised form 21 May 2020
Accepted 23 May 2020

Keywords:
Composite Column
Steel-Reinforced Concrete
Finite Element Model
Ductility Index
Load-Bearing Capacity
Eccentric Loading

ABSTRACT

Steel-reinforced concrete (SRC) columns, which are classified as composite columns, became the most widely used in recent years; because of their extensive advantages over the reinforced concrete and the steel columns. In this paper, the ductility index and its influential factors were explored to investigate the behavior of SRC columns. A straightforward approach was then proposed by establishing the necessary equations based on the plastic stress distribution method. Accordingly, an experimental program was performed on six SRC column specimens with two H- and cross-shaped steel sections and three eccentricity ratios of 0.4, 0.55, and 0.7. In addition, a finite element model was developed for numerical analysis using Abaqus software, which was verified by the experimental results. A total of 30 columns were thus analyzed for the parametric study where the effects of geometric and material variables, including steel percentage, concrete compressive strength, lateral tie spacing, and geometrical shape of the steel core on the ductility index of these columns were assessed. The results confirm that for the H-shaped column, reducing the lateral tie spacing ratio from 0.6 to 0.2 not only increases the ductility index to as much as 72%, it also induces a post-yield hardening in the load-displacement curve and increases the bearing capacity by 20%. Subsequently, load-bending moment interaction curves were developed according to plastic stress distribution method cited in EC4 Code and then compared with those obtained through the software. Thus, normalized curves were presented as a means to design these columns.

***doi**: 10.5829/ije.2020.33.08b.11*

1. INTRODUCTION

The application of SRC columns is particularly desirable due to many architectural, structural, and economic expediencies over the concrete or steel columns. Besides, the constant need to improve materials and reduce the dimensions and size required in the structural systems became critical, especially in high-rise buildings. In this context, SRC columns are utilized because of their high bearing capacity, high stiffness, and ductility. These columns, distinguished as a type of composite column, have significant advantages such as good shear strength, no local buckling of steel components, and proper fire resistance since the steel parts are encased within the concrete [1-5].

In recent years, numerous studies on composite columns have been carried out. For instance, the research done by An et al. [6], a numerical model was created in Abaqus to present a column containing an embedded steel tube section. The model was subsequently verified by experiment to evaluate the flexural performance of the column. Distinct regions of concrete confinement were also considered in modeling in order to improve accuracy. The steel tube sustained no local buckling, and developed its plastic strength. According to plastic stress distribution method, a relation was proposed to estimate flexural capacity of SRC sections. Ellobody et al. [7, 8] introduced different confinement regions into the numerical model using Abaqus by examining the SRC columns with H-shaped

*Corresponding Author Institutional Email: *m-naghi@nit.ac.ir* (M. Naghipour)

Please cite this article as: M. Ahmadi, M. Naghipour, M. Nematzadeh, Numerical and Experimental Investigations on the Behavior of SRC Columns Subjected to Eccentric Loading, International Journal of Engineering (IJE), IJE TRANSACTIONS B: Applications Vol. 33, No. 8, (August 2020) 1529-1543

steel section under the combination of axial load and bending moment. They demonstrated that incorporating such regions into numerical modeling leads to a good agreement between the experimental and numerical results. In their research, fixed rectangular zones were used to partition the confinement regions in numerical modeling. Lin and Chen [9] proposed a numerical model to estimate the bearing capacity of SRC columns with different I-, H-, cross-, and T-shaped sections and different lateral tie spacing. In this numerical model, two types of behavior were presented for the longitudinal reinforcement and the steel section. The method given by Mander et al. [10] was practiced to consider the effects of concrete confinement. The findings denoted that taking the impact of confinement into account would increase the load-bearing capacity of the column. Wang et al. [11] performed a numerical study via Abaqus on several SRC columns subjected to eccentric loading and verified the numerical model with the experimental results. A parametric study was then carried out to examine the factors counting the concrete strength, steel yield stress, and eccentricity of loading on the strength and behavior of these columns. The results were also compared with some regulations. The results indicated that the plastic stress distribution method, adopted by the codes, may not always be conservative. Han and An [12] studied the behavior of SRC columns with steel tube sections, emphasizing that the use of these sections in the construction of high-rise structures and bridges is perceived to be growing. They prepared a numerical model by Abaqus to study the behavior of the columns. The nonlinear behavior of the materials, as well as the interaction between the steel tube and the concrete, either the external part or the core concrete, were considered. Different regions of concrete confinement were defined in the software modeling so that three zones of highly-confined core concrete, moderately-confined steel tube exterior, and the unconfined concrete cover with distinct stress-strain behavior were included in the modeling. It was affirmed that the results obtained from the simulation were in good accord with the predicted values as a consequence of considering different regions of concrete confinement. A relationship was therefore recommended to estimate the bearing capacity of the column. Zhou et al. [13] conducted multiple numerical and experimental studies on the behavior of H-shaped steel sections of SRC columns subjected to eccentric compression. No less than eight specimens were tested to screen the effects of load eccentricity, width-to-thickness ratio of the steel section, and the shear studs. The results were put together with those of Abaqus modeling. In this regard, they exercised Li et al.'s [14] relationships to model the behavior of concrete in the software, considering the two confined and unconfined concrete regions. The outcomes exhibited a proper consistency between the measured values with those of the software predictions. Moreover, several analytical and experimental investigations have been previously conducted on the SRC columns with H- or cross-shaped sections, including Mirza and Skrabek [15], Mirza et al. [16], El-Tawil and Deierlein [17], Munoz and Hsu [18], Bogdan et al. [19], Lelkes and Gramblicka [20], among others.

According to literature so far, the behavior of SRC columns can be credited to several factors, one of which has been acknowledged to be the ductility. On this account, a number of SRC columns with different steel sections and load eccentricities were experimented in the present study. After the necessary tests and measurements, the specimens were modeled and validated through the Abaqus software, so that the proposed model could be used for further investigation. Afterward, a parametric study was accomplished on a total of 30 SRC columns, geometrical and material variables, including the section steel percentage, concrete compressive strength, lateral tie spacing, and the geometrical shape of steel section were discussed. Finally, some relationships were established to estimate the ductility index of columns with different steel sections. The required relationships for plotting the axial load-bending moment interaction curves of these columns were also derived based on the plastic stress distribution method. Furthermore, specific curves were presented, from which an inventory of SRC columns could be conveniently designed once these curves were generalized.

2. SUMMARY OF EXPERIMENTAL INVESTIGATION

Ahmadi et al. [21] performed an experimental and numerical study on six specimens of SRC columns. Figure 1 provides details of the experimental specimens. As it is inferred, the span length of all specimens is $460mm$, and the section dimensions are $150\times150mm$.The longitudinal reinforcement bars comprise $4\Phi10$, the ties are made of $\Phi8@60mm$, and the concrete cover thickness over the ties is $15mm$. As shown in this figure, grooved steel plates were used at both column ends so as to represent the hinged supports and apply different values of eccentricity ratios (e/B), including 0.4, 0.55 and 0.7. These experiments were performed in the structural laboratory of Noshirvani University of Babol, and thus, due to the limited load-bearing capacity of the testing device, such values were selected so that all specimens could be experimented.

It should be noted that the eccentricity, e, was measured relative to the plastic centroid of the section. Two types of steel sections were encased in the concrete, which makes up a total of 6 specimens given

the three eccentricity ratios. Table 1 summarizes the specimen specifications along with their notations.

A linear variable differential transformer (LVDT) was installed at midspan, perpendicular to column direction, to record the lateral displacement. Two other LVDTs were also instrumented on the sides of the specimen to measure the axial deformations. Mix design in preparing the concrete cylinders conformed to ACI211.1-91[22] with average 28-day compressive strength of 30MPa. Steel properties were determined according to the tension test recommended by ASTM E8/E8M[23], the results of which are reported in Table 2.

All laboratory specimens, with hinged boundary conditions at both ends, were subjected to eccentric compression. The overall schematic of the testing system, along with its boundary element, is given in Figure 2.

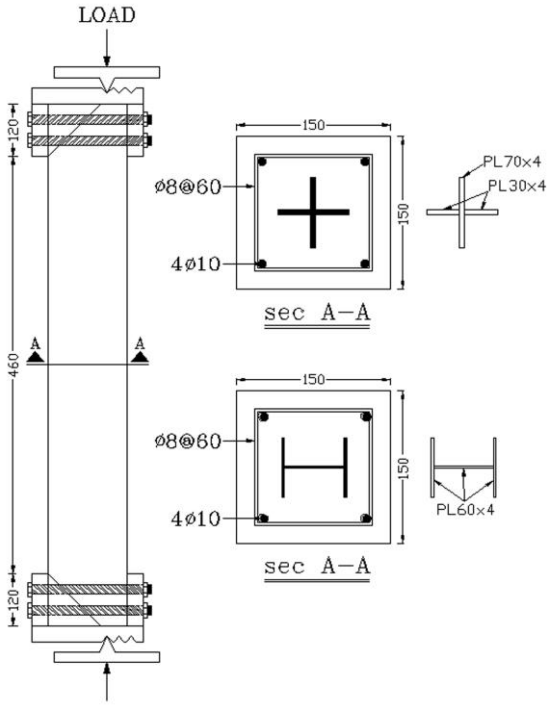

Figure 1. Overall dimensions of column with H- and cross-shaped sections

TABLE 1. Specifications of the tested SRC columns

Notation	Steel Core	Column Dimensions (mm)	Eccentricity (mm)
SRC-X60	Cross	150×150×700	60
SRC-X82	Cross	150×150×700	82.5
SRC-X105	Cross	150×150×700	105
SRC-H60	H	150×150×700	60
SRC-H82	H	150×150×700	82.5
SRC-H105	H	150×150×700	105

TABLE 2. Results of tensile test on plate and reinforcements

	Yield Stress (MPa)	Ultimate Stress (MPa)
Steel Plate	243	367
Longitudinal Rebar	302	430
Transvers Rebar	297	388

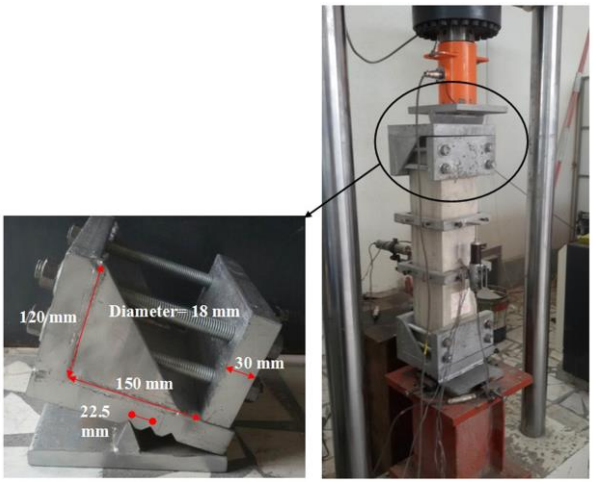

(a) Supporting plate to apply the eccentric load

(b) Overall testing system

Figure 2. Test setup with measuring arrangements

The results obtained for the SRC column with cross-shaped steel core in terms of three cases of eccentricity are sketched and compared in the form of axial load-axial displacement and axial load-midspan lateral displacement curves in Figure 3. In specimens SRC-X60 and SRC-X82, the ultimate yield and failure modes respectively happen to be cracking on the tensile face and concrete crushing on the compressive face at midspan. According to the figure, the load ramps up with a steep slope towards the peak load, while in specimen SRC-X105, there is an abrupt decline in the bearing capacity following the peak load, and thus the cracking and crushing occurs in the vicinity of the boundary element.

In like manner, the results of SRC columns with H-shaped steel core are illustrated in Figure 4. In specimens SRC-H60 and SRC-H82, the ultimate yield and failure modes, respectively, take place as cracking on the tensile face and crushing on the compressive face adjacent to the boundary element. In this sense, the post-peak capacity drops with a relatively sharp slope, whereas in specimen SRC-H105, yielding and failure occur at midspan. As lateral displacement gradually increases at midspan, the tensile reinforcement exceeds the yield limit strain.

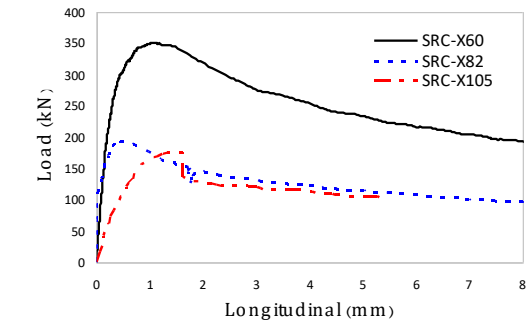

(a)

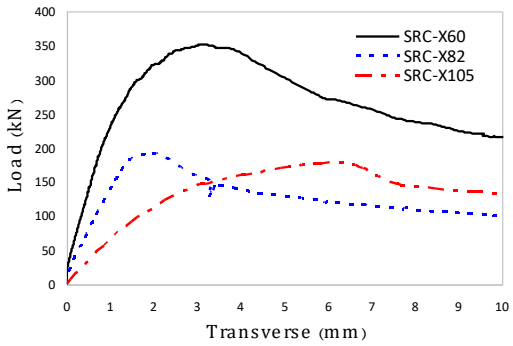

(b)

Figure 3. Laboratory specimens with cross-shaped steel core: (a)Axial load-longitudinal displacement curve; (b)Axial load-midspan lateral displacement curve

Figure 5 shows the failure mode in the ultimate state of all specimens.

3. FINITE ELEMENT ANALYSIS MODEL

The FE model developed in Abaqus, the steel section and the concrete were modeled using the S4R shell and C3D8R elements, respectively [24-25]. The three-

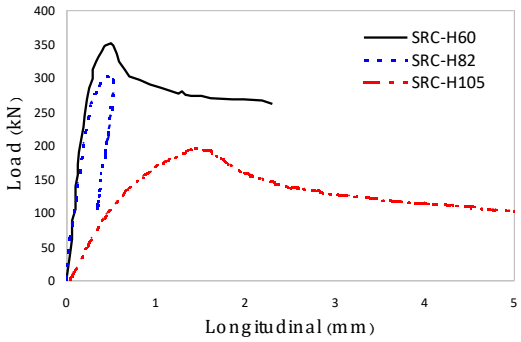

(a)

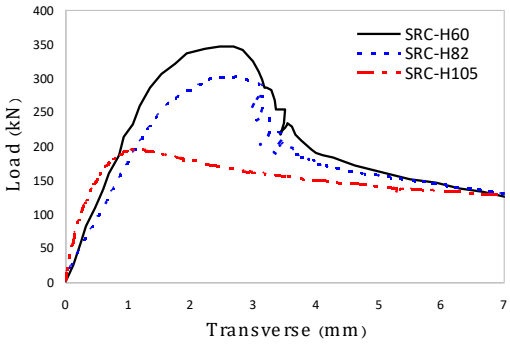

(b)

Figure 4. Laboratory specimens with H steel core: (a)Axial load-longitudinal displacement curve; (b)Axial load-midspan lateral displacement curve

dimensional two-noded T3D2 element was used for the simulation of longitudinal and lateral reinforcement bars. The steel components were embedded inside the concrete blocks to ensure an adequate bond between the steel sections, the concrete, and the reinforcements. Furthermore, the top and bottom of the specimen were supported by two rigid steel plates, to which R3D4 elements were selected and tied to the concrete surface in the defining step. The load was exerted to the top of the column with desired eccentricities in the displacement-control mode. The sketch of the numerical model is presented in Figure 6. In this model, the damaged plasticity model was implemented for the concrete material, which accounts for two fundamental principles of tensile cracking and compressive crushing during the failure mechanism. Besides $E = 4730\sqrt{f_c'}$ and $\nu = 0.2$ were postulated for concrete after the ACI318-11 [26], in which f_c' is the cylinder compressive strength in *MPa*. Also, the elastic-plastic model was adopted for steel material with $E = 200\ GPa$ and $\nu = 0.3$.

Figure 5. Ultimate yielding mode and failure of experimental specimens

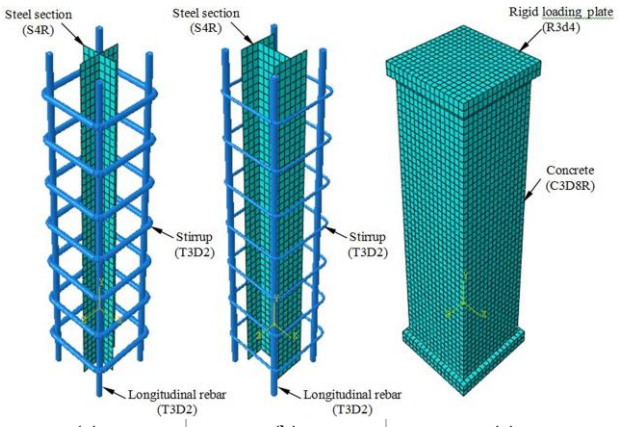

Figure 6. Finite element model of laboratory specimen: (a) cross-shaped section; (b) H-shaped section; (c) Overall configuration of the numerical model

The stress-strain behavior of the compression concrete was defined in the numerical model using the relations provided by Barr and Lee [27]. This model consists of a continuous function plus the sum of two exponential functions as given by Relation (1):

$$f_c(x) = C_1\left(e^{-C_2 x} - e^{-C_3 x}\right) \tag{1}$$

in which C_1, C_2, and C_3 are constants regulating the shape of the stress-strain curve and are calculated as follows:

$$x_{\max} = \frac{1}{C_3 - C_2}\ln\left(\frac{C_3}{C_2}\right) \tag{2}$$

$$C_1 = \frac{f_{\max}}{\left(\alpha^{\frac{1}{1-\alpha}} - \alpha^{\frac{\alpha}{1-\alpha}}\right)} \tag{3}$$

$$C_2 = \frac{\ln \alpha}{x_{\max}(\alpha - 1)} \tag{4}$$

where $f_{\max}$ is the uniaxial compressive strength, $x_{\max}$ the strain at ultimate load, and $\alpha = \frac{C_3}{C_2}$, which can be determined by Relation (5):

$$\begin{cases} \left(\frac{x_{\max}}{x_{0.2f_{\max}}}\right) \le 0.000572 \Rightarrow \alpha = 10^4 \\ 0.000572 < \left(\frac{x_{\max}}{x_{0.2f_{\max}}}\right) \le 0.026 \Rightarrow \alpha = 1.67\left(\frac{x_{\max}}{x_{0.2f_{\max}}}\right)^{-1.17} \\ 0.026 < \left(\frac{x_{\max}}{x_{0.2f_{\max}}}\right) \le 0.262 \Rightarrow \alpha = \sum_{i=0}^{6}\chi_i\left(\frac{x_{\max}}{x_{0.2f_{\max}}}\right)^i \\ \left(\frac{x_{\max}}{x_{0.2f_{\max}}}\right) \ge 0.262 \Rightarrow \alpha = 1.0001 \end{cases} \tag{5}$$

The above relationships, $x_{0.2f_{\max}}$ is the strain corresponding to 20% of the uniaxial compressive stress in the post-peak phase. The stress-strain relationships recommended by An et al. [6] is presented in Relation (6) to model the behavior of concrete in tension:

$$\frac{\sigma_t}{\sigma_{t0}} = \frac{\varepsilon_t/\varepsilon_{t0}}{0.31\sigma_{t0}^2\left[\left(\varepsilon_t/\varepsilon_{t0}\right) - 1\right]^{1.7} + \varepsilon_t/\varepsilon_{t0}} \tag{6}$$

where $\varepsilon_{t0} = \sigma_{t0}/E_C$, and the tensile cracking resistance σ_{t0} is estimated by $\sigma_{t0} = 1.4\left(f_c'/10\right)^{0.67}$ in which $E_C = 4730\sqrt{f_c'}$, and f_c' is the cylinder compressive strength is in *MPa*.

4. VERIFICATION OF FINITE ELEMENT MODEL

The numerical predictions were compared with those of the experiment to verify the proposed FE model. The comparison was made respecting the three columns of SRC-H105, SRC-X82, and SRC-X60 with specifications reported in Table 1; the results of which were then employed for verification of the numerical models.

4. 1. Axial Load-Axial Displacement Behavior The experimental results were compared with those obtained via FE modeling in terms of load-displacement behavior, as depicted in Figure 7. As for the three verified specimens, the load-axial displacement curves match the FE curves with a subtle difference at peak load, which is likely to be associated with a geometric and loading defect/imperfection generated through the experiment.

4. 2. Axial Capacity The ultimate axial loads were obtained from the numerical model and compared with those of the experiment. Table 3 compares the peak load of the laboratory specimens with the capacity derived from the FE analysis. The reported mean and standard deviation values highlight a favorable efficiency of the FE model in predicting the desired measures.

4. 3. Failure Modes The main yielding mode in the experimental specimens was the concrete crushing. Surface cracks in concrete are always an indication of reaching the yield state. The failure sequence of the tested columns started with cracking in the middle of the column as well as the top and bottom regions close to supports. Then, as the load increased, cracks became wider and the concrete cover spalling happened. Finally, concrete crushing began, followed by the yielding of the longitudinal rebars. The yielding modes of the SRC

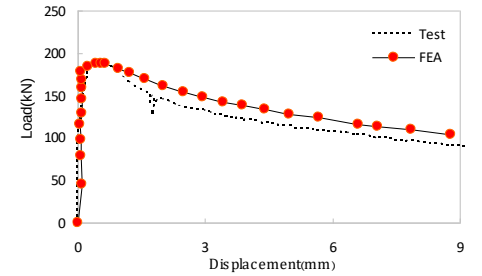

(a)

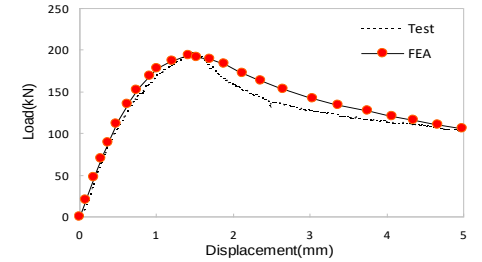

(b)

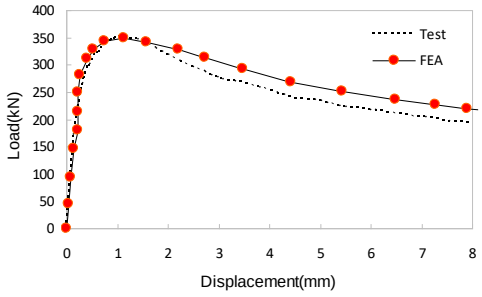

(c)

Figure 7. Comparison of load-longitudinal displacement: (a) SRC-X82; (b) SRC-H105; (c) SRC-X60.

TABLE 3. Comparison of the numerical and experimental results

Sample codes	Peak load(kN)		$\frac{P_{num}}{P_{exp}}$
	P_{exp}	P_{num}	
SRC-H105	196.1	193.2	0.985
SRC-X82	193.2	188.3	0.975
SRC-X60	351.1	348.6	0.993
Mean			0.984
Standard deviation			0.009

columns obtained from the finite element analysis were compared with those of the experimental specimens. A comparison between the yielding modes of experimental and numerical columns is demonstrated in Figure 8.

5. ANALYSIS AND DISCUSSIONS

Once validity of the numerical model was established, ensuring the behavioral model of materials, the correct interaction between different element parts, as well as the applied boundary conditions and loading procedure, a parametric study was embarked on by varying the geometric and material properties of the model so as to better understand the behavior of SRC columns. In this setting, the influence of several factors, embracing steel percentage, concrete compressive strength, lateral tie

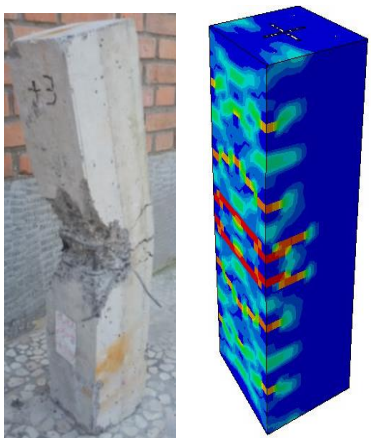

(a)

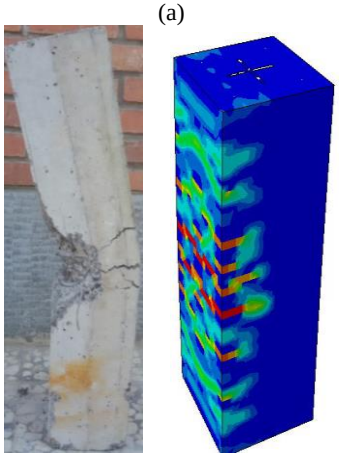

(b)

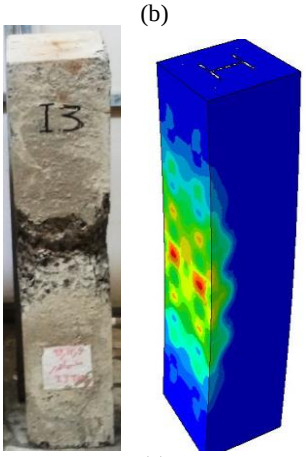

(c)

Figure 8. Comparison of yielding modes and failure of experimental and numerical specimens: (a) SRC-X60 column; (b) SRC-X82 column; (c) SRC-H105 column

spacing, and geometrical shape of steel sections were tackled. Thus, a total of 30 SRC columns were analyzed (as shown in Figure 9), the results of which are given in Tables 4, 5, and 6 accompanied by the specimens' specifications. In these tables, L denotes the specimen length, D the column side, S the lateral tie spacing, A_s the steel percentage, and f_c the standard cylinder compressive strength. In a general sense, both the high percentage of section steel and the low tie spacing enhance the ductility of the column. As a criterion to examine the ductility of SRC columns in this paper, the ductility index (μ) is defined as the ratio of displacement at a point corresponding to 85% of the peak load on the descending branch of the curve (Δu) to the yield point displacement (Δ_y) [28]:

$$\mu = \frac{\Delta_u}{\Delta_y} = f(A_s, f_c, \frac{S}{D}, steel\ core\ shape) \quad (7)$$

It is important to note that in the modeling settled by the Abaqus software, the possible slip between the steel section and the concrete surface, as well as the geometrical defects generated during the experiment, are not taken into account. Moreover, this research does not pursue the code recommendations at selecting the material properties and section dimensions, which can be regarded as a drawback to this study.

As reported in Table 4, the ductility index increases with an increase in the steel percentage of the section. In this table, three values of 1, 3, and 5% were assumed for the steel percentage. The ductility index marks the highest measure for the box-shaped section and the lowest value for the cross-shaped. It is discerned, based on the tabulated results, that the ductility index is escalated by 31.7% as the steel percentage of the H-shaped section increases from 1 to 5%. Such a gain is as much as 14.7 and 25% for the cross- and box-shaped sections, respectively.

The obtained results match the eccentricity ratio of 0.1, in which case the behavior of the column is closer to that of the steel, and thus, μ increases by increasing the steel percents (As).

Figure 10 illustrates the load-axial displacement curve of various sections for different percentages of steel. It is recognized that the box-shaped column features a higher bearing capacity in the post-yield phase than the other sections. This argument is connected with the higher confinement of concrete inside the box-shaped steel section, which in turn increases the ductility index. In some measure, the fact holds for the H-shaped section, owing to the confinement of concrete between the flanges and the web.

Three values of 15, 30, and 60 *MPa* were adopted for concrete compressive strength in Table 5 so as to evaluate its impact on the ductility index. It turns out that the ductility index downscales with increasing compressive strength of concrete such that in H-shaped section, the ductility index reduced by 38.4% as the compressive strength surged from 15 to 60 *MPa*. The commensurate values for the cross- and box-shaped sections were 32.4 and 26.2%, respectively. The obtained results match the eccentricity ratio of 0.1, in which case, similar to the column under axial load, an increase in fc makes the column to have a more brittle response.

Figure 11 depicts the load-axial displacement curve of various sections for different values of concrete compressive strength. As can be seen, the ultimate axial

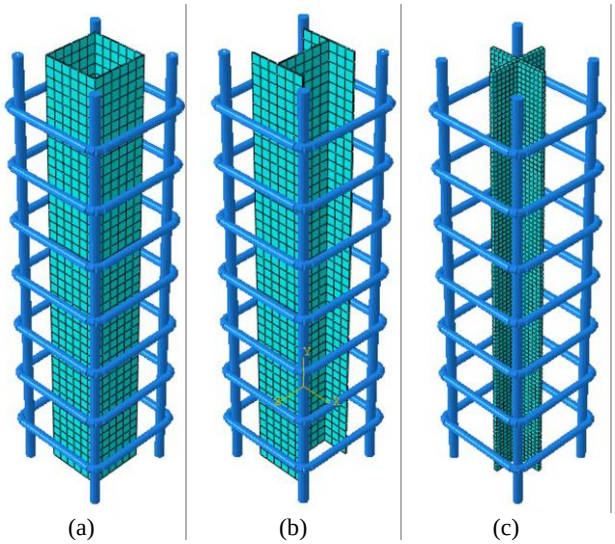

(a) (b) (c)

Figure 9. Sections used in the parametric study: (a) Box-shaped section; (b) H-shaped section; (c) Cross-shaped section removed

TABLE 4. Effect of steel percentage (As) on the column ductility index

Specimen	Steel Section (mm)	A_s (%)	Axial Capacity (kN)	Δ_y (mm)	Δ_u (mm)	μ
HN1	$3PL60\times1.25$	1	765.8	0.95	2.105	2.21
HN2	$3PL60\times3.75$	3	877.1	1	2.51	2.51
HN3	$3PL60\times6.25$	5	991.7	1.1	3.2	2.91
XN4	$2PL60\times1.91$	1	764.2	0.9	1.966	2.18
XN5	$2PL60\times5.92$	3	873.7	0.95	2.255	2.37
XN6	$2PL60\times10.25$	5	983.5	1	2.5	2.5
BN7	$60\times60\times0.95$	1	771.8	1	2.4	2.4
BN8	$60\times60\times2.95$	3	884.8	1	2.81	2.81
BN9	$60\times60\times5.12$	5	1004.3	1.25	3.75	3

* Column Dimensions (mm):150×150×460, L/D=3, S/D=0.4, f_c=30MPa, e/B=0.1

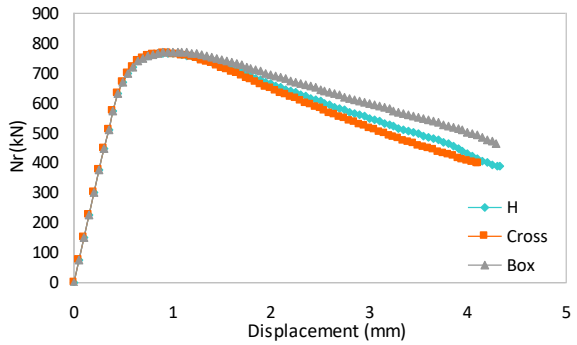

(a)

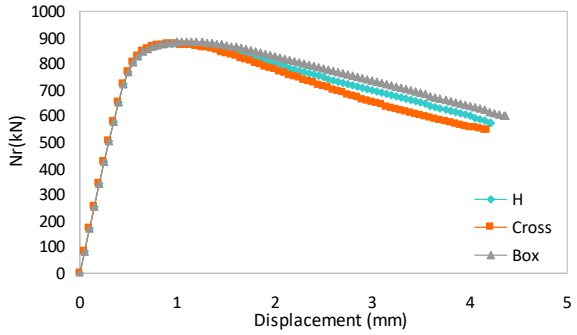

(b)

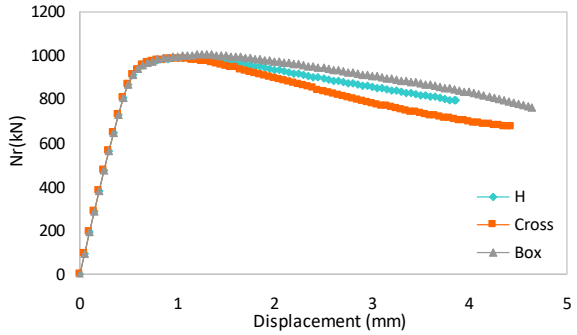

(c)

Figure 10. Comparison of load-axial displacement curves for column with various steel cores: (a) As=1%; (b) As=3%; (c) As=5%

TABLE 5. Effect of concrete compressive strength (fc) on the column ductility index

Specimen	A_s (%)	f_c (MPa)	Axial Capacity (kN)	Δ_y (mm)	Δ_u (mm)	μ
HL10	3	15	602.7	1.25	4.22	3.36
HN11	3	30	877.1	1	2.51	2.51
HH12	3	60	1448.8	0.85	1.763	2.07
XL13	3	15	597.7	1.2	3.45	2.87
XN14	3	30	873.7	0.95	2.255	2.37
XH15	3	60	1449.4	0.85	1.65	1.94
BL16	3	15	617.5	1.5	4.47	2.98
BN17	3	30	884.8	1	2.81	2.81
BH18	3	60	1449.3	0.85	1.863	2.2

* Column Dimensions (mm):150×150×460, L/D=3, S/D=0.4, e/B=0.1

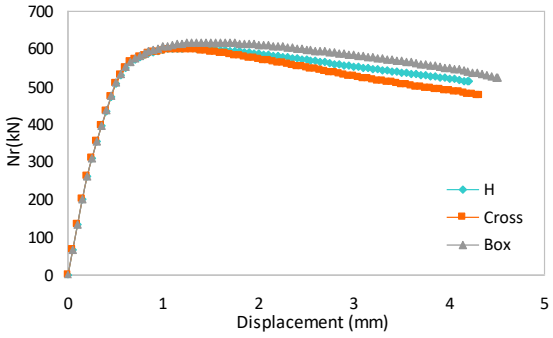

(a)

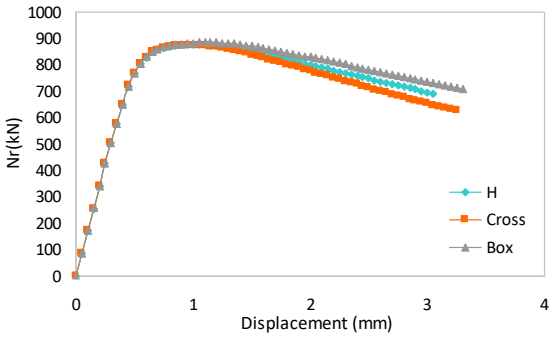

(b)

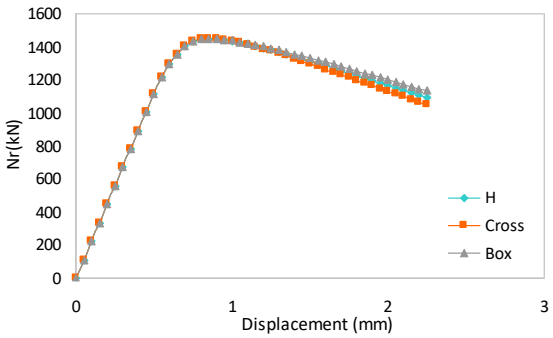

(c)

Figure 11. Comparison of load-axial displacement curves for column with various steel cores: (a) fc=15 MPa; (b) fc=30 MPa; (c) fc=60 MPa

load and the stiffness of the column were affected by concrete strength such that the curve captures a steep slope in the ascending portion as regards to the higher strength concrete and due to high elastic modulus. The descending portion of the curve takes even a steeper slope because of the brittleness of the section, which

reduces its ductility index compared to sections with lower compressive strengths.

Table 6 outlines the effect of tie spacing on the column ductility index, for which four values of spacing ratios 0.1, 0.2, 0.4, and 0.6 have been considered. It is well comprehended that the main objective of using ties in columns is to provide concrete confinement, to trigger suitable support for longitudinal bars so as to prevent their buckling, and to improve the shear strength of the section. Accordingly, the tie spacing is an influential factor on the ultimate capacity and the behavior of columns. Table 6 demonstrates that a reduction in the tie spacing increases the ductility index, characterizing the highest value for the box-shaped section and the lowest measure for the cross-shaped. The results also signify that with increasing tie spacing, the bearing capacity and the ductility index drastically fall. In this case, by varying spacing ratio (S/D) from 0.1 to 0.6 for the H-shaped section, the ductility index drops by 54.6%. The equivalent values are 56 and 51.4% for the cross- and box-shaped sections.

Figure 12 portrays the load-axial displacement curves concerning the different values of S/D. As can be seen, the ascending branch of the curves is identical for all columns and the discrepancy between different sections, influenced by the tie spacing, is observed in the post-yield phase so that there is a post-yield hardening area at spacing ratios of 0.1 and 0.2. This is mainly attributable to the evolution of high confinement and the reinforcement buckling prevention as per the lateral ties. Such impact subsides as the spacing increases, followed by a decline in the curve slope and subsequently a decrease in the bearing capacity and the ductility index.

Figure 12, for S/D= 0.1 and 0.2, due to the high confinement induced by the ties and the inhibition of the buckling of longitudinal bars, there is a post-yield hardening zone, and thus, the strength is significantly increased. Meanwhile, in the plotted curves, the criterion for calculating the ductility index, according to literature [28], the displacement is at 85% of the peak load in the descending branch, and hence, the end point of the curve does not indicate the failure point, and simply the curve continues based on the software output.

TABLE 6. Effect of tie spacing (S/D) on the column ductility index

Specimen	A_s (%)	$\frac{S}{D}$	Axial Capacity (kN)	Δ_y (mm)	Δ_u (mm)	μ
HN19	3	0.1	1163.45	0.7	3.69	5.27
HN20	3	0.2	1014.86	0.75	3.09	4.12
HN21	3	0.4	877.1	1	2.51	2.51
HN22	3	0.6	845.6	0.9	2.15	2.39
XN23	3	0.1	1160.4	0.7	3.55	5.07
XN24	3	0.2	1015.2	0.75	2.86	3.81
XN25	3	0.4	873.7	0.95	2.255	2.37
XN26	3	0.6	841.1	0.85	1.901	2.23
BN27	3	0.1	1176.1	0.7	3.862	5.52
BN28	3	0.2	1025.4	0.75	3.3	4.4
BN29	3	0.4	884.8	1	2.81	2.81
BN30	3	0.6	848.4	0.9	2.411	2.68

* Column Dimensions (mm):150×150×460, L/D=3, f_c=30MPa, e/B=0.1

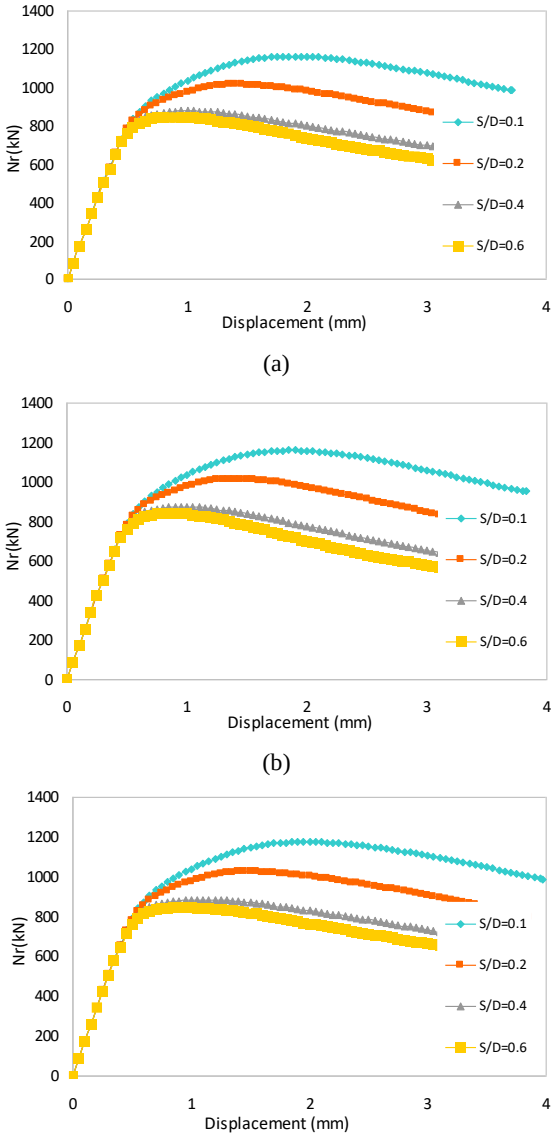

Figure 12. Load-axial displacement curves for column with various steel cores wrt different S/D ratios: (a) H-shaped section; (b) Cross-shaped section; (c) Box-shaped section

Based on the factors affecting the ductility index and the obtained results, appropriate relationships can be established for the ductility index of the H-, cross-, and box-shaped columns as follows:

$$\mu_H = \left[60.203 + 1308.34A_s - 2.931 f_c\right] \times \left(\frac{S}{D}\right)^2 + 125(A_s)^2 + 0.00726(f_c)^2 - 16.611A_s . f_c \times \left(\frac{S}{D}\right) \quad (8)$$

$$\mu_{Cross} = \left[55.047 + 1578.125A_s - 2.813 f_c\right] \times \left(\frac{S}{D}\right)^2 - 75(A_s)^2 + 0.00751(f_c)^2 - 20A_s . f_c \times \left(\frac{S}{D}\right) \quad (9)$$

$$\mu_{Box} = \left[69.693 + 1401.04A_s - 3.363 f_c\right] \times \left(\frac{S}{D}\right)^2 - 275(A_s)^2 + 0.00789(f_c)^2 - 16.056A_s . f_c \times \left(\frac{S}{D}\right) \quad (10)$$

In the above relations, A_s is the ratio of section steel area, f_c the cylinder compressive strength in *MPa*, S the tie spacing, and D is the sectional side in *mm*. It should be noted that the above relations are limited to when $\frac{e}{B} = 0.1$, $f_c \geq 30MPa$ and $\frac{S}{D} \leq 0.4$. Three steel percentages of 1, 3, and 5% were assumed in plotting the axial load-bending moment interaction curves.

A total of six eccentricities, i.e., e/B= 0, 0.1, 0.2, 0.4, 0.8, and 2 were chosen to develop each interaction curve in Abaqus. The generated curves were then compared with the concrete section without the steel core. The dimensions selected for plotting the interaction curves are similar to those of laboratory specimens, yet differences in types and percentages of steel core. Figure 13 sketches the axial load-bending moment interaction curves for the cross-, H-, and box-shaped sections with three steel core percentage ratios of $A_S = 1$, 3, and 5%. The mentioned curves have been compared with that of the concrete section without the steel core for different values of steel core percentages.

It is proved that the interaction curves converge as for the cross-shaped column specifically at the balance point for 1 and 3% of steel. However, with increasing steel percentage to 5%, contours scatter especially at the balance point. Nevertheless, in the H-shaped column, the curves are close to each other in the compression-dominated region for the 3 and 5% of steel, though after the balance point, in the tension-dominated region, the curve related to 3% of steel approaches that of the 1% of steel. On the contrary, contours maintain relatively identical distances throughout the curve in the box-shaped section for different steel percentages.

As shown in the figure, the performance of H-, cross-, and box-shaped columns with A_s=1% is almost identical. As the steel percentage rises to A_s=3%,

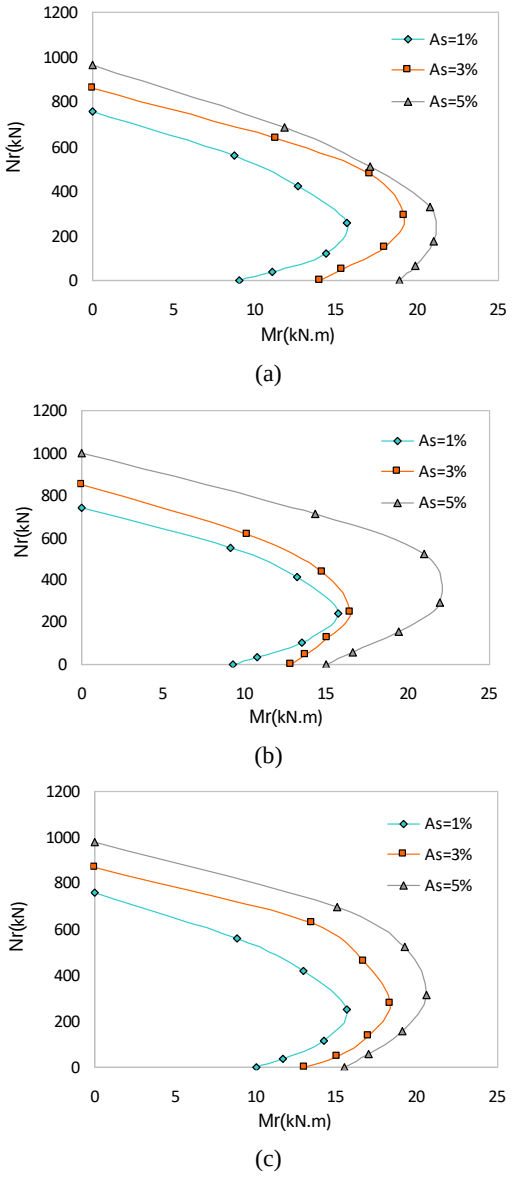

Figure 13. Interaction curves for column with different steel sections: (a) H-shaped section; (b) Cross-shaped section; (c) Box-shaped section

columns with H- and box-shaped sections demonstrate similar performances, whose curves possess more extensive areas as to the cross-shaped section. However, there is a shift in the trend as the steel percentage reaches A_s=5%. Interestingly, Figure 14 reveals that the box- and cross-shaped sections are comparable in performance in the compression- and tension-dominated regions. Yet, they perform unlike at the balance region, wherein the cross-shaped section marks a larger balance point. Furthermore, the H-shaped section sustains lower bearing capacity in the compression-dominated region and higher capacity in the tension-dominated zone when compared to the other two sections.

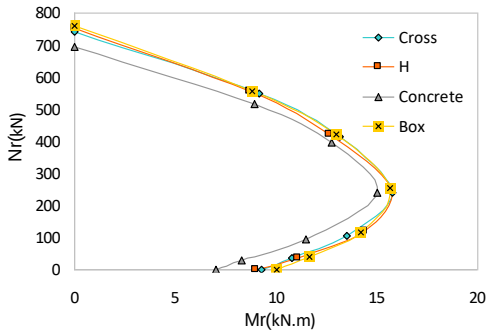

(a)

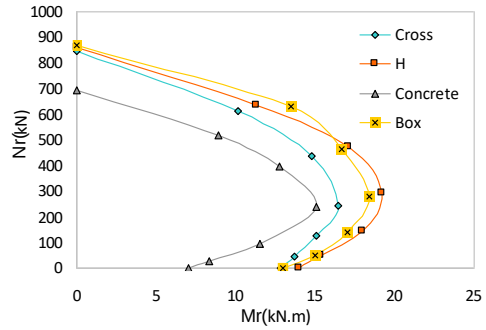

(b)

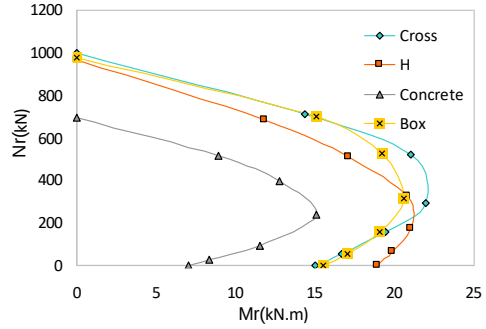

(c)

Figure 14. Comparison of interaction curves for column with different steel sections: (a) As=1%; (b) As=3%; (c) As=5%

In order to develop the interaction curves according to EC4 recommendations and compare them with numerical results, a specimen with an H-shaped section with dimensions and steel percentage similar to that of the laboratory sample was designated. The interaction curve in this code has been simplified to a polygon curve, so that in this study, the points required for plotting the interaction curves were computed based on the plastic stress distribution equations. The nominal compressive strength can be expressed by Relation (11):

$$P_{n0} = F_y.A_s + c_2.f_c(A_c + A_{sr}\frac{E_s}{E_c}) \quad (11)$$

Based on the plastic stress distribution concept, the flexural capacity, M_{max}, related to the balance point, which is larger than the pure flexure, can be calculated as the Relation (12) for the SRC with an H-shaped section around the strong axis and the reinforcements laid at both sides. In this case, the column is simultaneously subjected to bending and axial compression, and the plastic neutral axis lies at the center of the cross-section.

$$M_{max} = \frac{1}{8}c_2.f_c.A_c.h + F_y.A_s.d.\left[\frac{4A_f + A_w}{8A_f + 4A_w}\right] + \frac{1}{2}A_{sr}.F_{ysr}.(h-2d') \quad (12)$$

In the above relation, $A_c = b.h - A_s - A_{sr}$ is the net concrete area, $A_f = b_f \times t_f$ the H-shaped section flange area, $A_w = d \times t_w$ the web area, d the section height, and d′ is the distance from the centerline of the rebars to the nearest outer face of the column, A_{sr} and F_{ysr} are the area of reinforcements and their yield stress, respectively. The flexural capacity of the section can be calculated according to the plastic stress distribution method based on Figure 15. As it is observed, in this case, the plastic neutral axis is located above the center of the cross-section. Accordingly, the nominal flexural strength of the SRC column with an H-shaped section around the strong axis and with reinforcement placed at both sides is calculated as the following relations:

$$if \quad h_n = \frac{A_c}{2(b-t_w) + \frac{4F_y.t_w}{c_2.f_c}} \le \frac{h_w}{2} \quad \Rightarrow$$

$$M = \frac{1}{4}c_2.f_c\left[A_c - 2h_n(t_w - b)\right](\frac{h}{2} - h_n) + \frac{1}{2}A_{sr}.F_{ysr}(h-2d') + F_y.A_f(d-2t_f) + F_y.A_w(\frac{d}{4} - t_f) + F_y.t_w(h_n^2 + t_f^2) \quad (13)$$

$$if \quad \frac{h_w}{2} < h_n = \frac{c_2.f_c.b.h + 2F_y.b_f.d - 2F_y.A_s}{4F_y.b_f + 2c_2.f_c.b} \le \frac{d}{2} \quad \Rightarrow$$

$$M = \frac{1}{2}c_2.f_c.b.(\frac{h}{2} - h_n)^2 + \frac{1}{2}A_{sr}.F_{ysr}(h-2d') + F_y.A_f(2h_n + d) + F_y.b_f(h_n - \frac{d}{2})^2 + F_y.A_w(\frac{d}{2} - h_n) \quad (14)$$

$$if \quad h_n = \left[\frac{h}{2} - \frac{A_s.F_y}{c_2.f_c.b}\right] > \frac{d}{2} \quad \Rightarrow$$

$$M = \frac{1}{2}c_2.f_c.b.(\frac{h}{2} - h_n)^2 + A_s.F_y.h_n + \frac{1}{2}A_{sr}.F_{ysr}(h-2d') \quad (15)$$

where h_w is the net height of the H-shaped section.

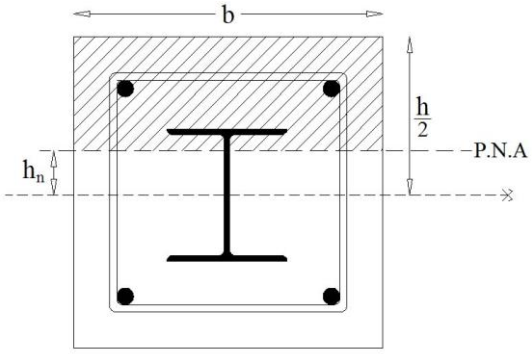

Figure 15. Column section for calculating the flexural capacity

Based on the calculations performed using the method stated in the code, and with the aid of the above relationships, as well as considering the numerical modeling of the experimental specimen, it is confirmed that the relations derived from the plastic stress distribution method are in favorably good agreement with the numerical model. The only conservative exception is witnessed at the axial compression and part of the compression-dominated region, which is shown in Figure 16.

Figures 17 and 18 illustrate the normalized interaction curves of the column with different section steel percentages and longitudinal reinforcement. In these curves, $\rho_{sr}=\frac{A_{sr}}{b.h}$ is the percentage of longitudinal reinforcement, $\rho_s=\frac{A_s}{b.h}$ the section steel percentage, N_{ro} the pure axial capacity, M_{ro} the pure flexural capacity, and $\gamma=\frac{h-2d'}{h}$. It is noted that these curves reflect the reciprocal influence of the rectangular and the H-shaped sections around the strong axis, with rebars distributed

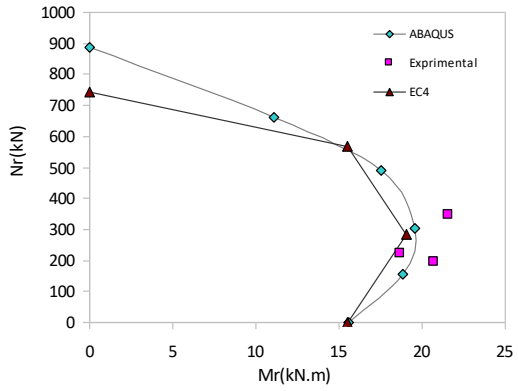

Figure 16. Comparison of the interaction curves for the column with H-shaped section and steel percentage of $A_s=3.2\%$

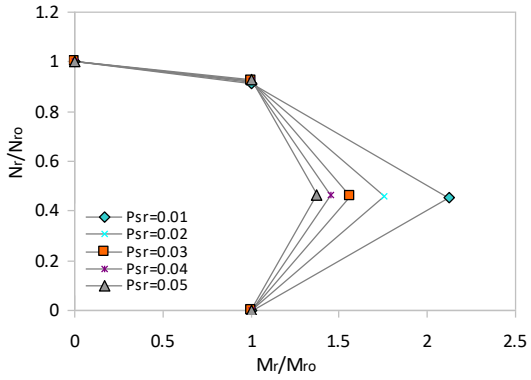

(a)

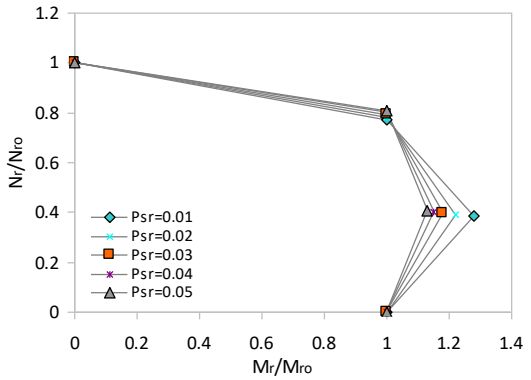

(b)

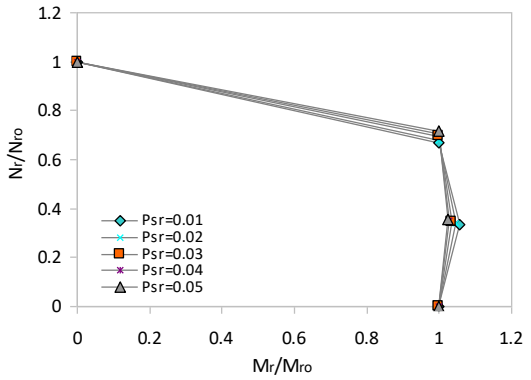

(c)

Figure 17. Normalized interaction curves for the H-shaped column in terms of ultimate strength for $\gamma=0.6$: (a) $\rho_s=0.01$; (b) $\rho_s=0.03$; (c) $\rho_s=0.05$

at both sides of the section. In Figure 17, the curves have been plotted in terms of the ultimate capacity $\frac{N_r}{N_{ro}}$ and $\frac{M_r}{M_{ro}}$. As shown in this figure, with increasing steel percentage, the maximum moment corresponding to the balance point approximately approaches the flexural capacity of the cross-section, and thus the curves overlie

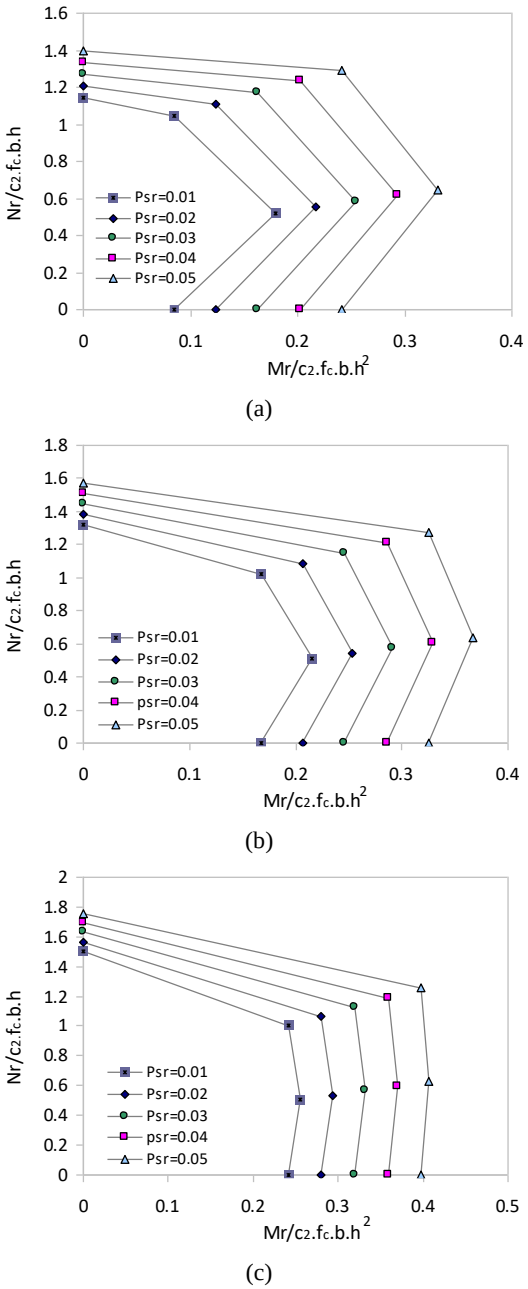

Figure 18. Normalized interaction curves for the H-shaped column in terms of concrete strength for $\gamma = 0.6$: (a) $\rho_s = 0.01$; (b) $\rho_s = 0.03$; (c) $\rho_s = 0.05$

for different percentages of longitudinal reinforcement. This specifies that as the steel core becomes stronger, the impact of the longitudinal reinforcement on the flexural capacity of the cross-section is mitigated, which is not the case for the lower percentages of section steel. In Figure 18, the normalized curves have been developed in terms of concrete strength $\frac{N_r}{c_2 . f_c . b.h}$ and $\frac{M_r}{c_2 . f_c . b.h^2}$. In this figure, as the steel percentage increases, the curves take a bi-linear form, and the balance point moment approximates the pure flexural capacity. By generalizing such curves for different values of γ and rebars positioned at four sides of the column section, more inclusive curves can be obtained for the design purpose of these columns.

6. CONCLUSION

The present study aimed to investigate the behavior of SRC columns subjected to the combination of axial load and bending moment. The conclusionss were drawn as follows:

1. As the steel percentage of the cross-section increases, the ductility index surges such that a rise in the steel percentage from 1 to 3% and from 3 to 5%, respectively, escalate the ductility index by 13.6 and 16%. The corresponding values are 8.7 and 5.5% for the cross-shaped section, and 17.1 and 6.8% for the box-shaped section.
2. With increasing concrete compressive strength, the ductility index decreases so that in columns with H-shaped sections, an escalation in the compressive strength from 15 to 60 *MPa* reduces the ductility index by 38.4%. Such a reduction is 32.4% for the cross-shaped and 26.2% for the box section.
3. As the lateral tie spacing increases, the bearing capacity and the ductility index sharply dropped, in such a way that by varying the spacing ratio from 0.1 to 0.6 for the H-shaped section, the ductility index slumped by 54.6%. The equivalent values are 56 and 51.4% for the cross-shaped and box-shaped sections.
4. The performance of columns with cross-, H-, and box-shaped steel cores is akin when $A_S = 1\%$, and the axial load-bending moment interaction curves roughly coincide.
5. As the steel percentage is raised to $A_S = 3\%$, the box- and H-shaped sections conform in performance. In this case, the axial load-bending moment interaction curves retain more extensive areas and higher distances, compared to that of the cross-shaped section, especially at the balance point.
6. Each of the studied sections features a distinct performance at $A_S = 5\%$ such that the box- and cross-shaped columns are analogous in the compression- and tension-dominated regions. Yet, they are different in the vicinity of the balance point in that the cross-shaped column captures a larger balance point. The column with an H-shaped steel core gains a lower bearing capacity in the compression-dominated region, though

its bearing capacity in the tension-dominated region excels, as compared to the other two sections.

7. It is perceptible in the normalized interaction curves, for column with the H-shaped section and $\rho_s = 0.01$, that the normalized moment $\frac{M_r}{M_{ro}}$, corresponding to the balance point of a section with $\rho_{sr} = 0.01$ is by 35.4% larger than that of a section with $\rho_{sr} = 0.05$.

8. It is noticeable in the normalized interaction curves, for column with the H-shaped section and $\rho_s = 0.03$, that the normalized moment $\frac{M_r}{M_{ro}}$, corresponding to the balance point of a section with $\rho_{sr} = 0.01$ is by 11.7% larger than that of a section with $\rho_{sr} = 0.05$.

9. It is visible in the normalized interaction curves, for column with the H-shaped section and $\rho_s = 0.05$, that the normalized moment $\frac{M_r}{M_{ro}}$, corresponding to the balance point of a section with $\rho_{sr} = 0.01$ is by 3.3% larger than that of a section with $\rho_{sr} = 0.05$.

10. The normalized interaction curves of short columns with the H-shaped section and $\gamma = 0.6$, provide a straightforward approach in designing the cited columns, where the generalization of such curves for various values of γ and the reinforcement placed at four sides of the column would contribute to even more developed curves.

7. ACKNOWLEDGEMENTS

The present study was conducted under the grant number BNUT925940001 at Babol Noshirvani University of Technology, which is hereby greatly appreciated.

8. REFERENCES

1. Shariati, M., Sulong, N.R., Shariati, A. and Kueh, A., "Comparative performance of channel and angle shear connectors in high strength concrete composites: An experimental study", ***Construction and Building Materials***, Vol. 120, (2016), 382-392 DOI: https://doi.org/10.1016/j.conbuildmat.2016.05.102.
2. Rahmani, Z., Naghipour, M. and Nematzadeh, M., "Flexural performance of high-strength prestressed concrete-encased concrete-filled steel tube sections", ***International Journal of Engineering***, Vol. 32, No. 9, (2019), 1238-1247 DOI: https://doi:10.5829/ije.2019.32.09c.03.
3. Nematzadeh, M., Naghipour, M., Jalali, J. and Salari, A., "Experimental study and calculation of confinement relationships for prestressed steel tube-confined compressed concrete stub columns", ***Journal of Civil Engineering and Management***, Vol. 23, No. 6, (2017), 699-711 DOI: https://doi.org/10.3846/13923730.2017.1281837.
4. ECS, "Eurocode 4: En 1994-1-2: 2004: Design of composite steel and concrete structures. Part1-1: General rules–structural rules for buildings, ECS Brussels, Belgium, (2004).
5. An, Y.-F., Han, L.-H. and Roeder, C., "Performance of concrete-encased cfst box stub columns under axial compression", ***Structures***, Vol. 3, (2015), 211-226 DOI: https://doi.org/10.1016/j.istruc.2015.05.001.
6. An, Y.-F., Han, L.-H. and Roeder, C., "Flexural performance of concrete-encased concrete-filled steel tubes", ***Magazine of Concrete Research***, Vol. 66, No. 5, (2014), 249-267 DOI: https://doi.org/10.1680/macr.13.00268.
7. Ellobody, E., Young, B. and Lam, D., "Eccentrically loaded concrete encased steel composite columns", ***Thin-walled Structures***, Vol. 49, No. 1, (2011), 53-65 DOI: https://doi.org/10.1016/j.tws.2010.08.006.
8. Ellobody, E. and Young, B., "Numerical simulation of concrete encased steel composite columns", ***Journal of Constructional Steel Research***, Vol. 67, No. 2, (2011), 211-222 DOI: https://doi.org/10.1016/j.jcsr.2010.08.003.
9. Chen, C.-C. and Lin, N.-J., "Analytical model for predicting axial capacity and behavior of concrete encased steel composite stub columns", ***Journal of Constructional Steel Research***, Vol. 62, No. 5, (2006), 424-433 DOI: https://doi.org/10.1016/j.jcsr.2005.04.021.
10. Mander, J.B., Priestley, M.J. and Park, R., "Theoretical stress-strain model for confined concrete", ***Journal of Structural Engineering***, Vol. 114, No. 8, (1988), 1804-1826 DOI: https://doi.org/10.1061/(ASCE)0733-9445(1988)114:8(1804).
11. Wang, H., Li, J. and Song, Y., "Numerical study and design recommendations of eccentrically loaded partially encased composite columns", ***International Journal of Steel Structures***, Vol. 19, No. 3, (2019), 991-1009 DOI: https://doi.org/10.1007/s13296-018-0179-7.
12. Han, L.-H. and An, Y.-F., "Performance of concrete-encased cfst stub columns under axial compression", ***Journal of Constructional Steel Research***, Vol. 93, (2014), 62-76 DOI: https://doi.org/10.1016/j.jcsr.2013.10.019.
13. Zhou, X., Yan, B. and Liu, J., "Behavior of square tubed steel reinforced-concrete (src) columns under eccentric compression", ***Thin-walled Structures***, Vol. 91, (2015), 129-138 DOI: https://doi.org/10.1016/j.tws.2015.01.022.
14. Li, B., Park, R. and Tanaka, H., "Stress-strain behavior of high-strength concrete confined by ultra-high-and normal-strength transverse reinforcements", ***ACI Structural Journal***, (2001), 395-406 DOI:http://hdl.handle.net/10220/8359.
15. Mirza, S.A. and Skrabek, B., "Statistical analysis of slender composite beam-column strength", ***Journal of Structural Engineering***, Vol. 118, No. 5, (1992), 1312-1332 DOI: https://doi.org/10.1061/(ASCE)0733-9445(1992)118:5(1312).
16. Mirza, S.A., Hyttinen, V. and Hyttinen, E., "Physical tests and analyses of composite steel-concrete beam-columns", ***Journal of Structural Engineering***, Vol. 122, No. 11, (1996), 1317-1326 DOI: https://doi.org/10.1061/(ASCE)0733-9445(1996)122:11(1317).
17. El-Tawil, S. and Deierlein, G.G., "Strength and ductility of concrete encased composite columns", ***Journal of Structural Engineering***, Vol. 125, No. 9, (1999), 1009-1019 DOI: https://doi.org/10.1061/(ASCE)0733-9445(1999)125:9(1009).
18. Munoz, P.R. and Hsu, C.-T.T., "Behavior of biaxially loaded concrete-encased composite columns", ***Journal of structural engineering***, Vol. 123, No. 9, (1997), 1163-1171 DOI: https://doi.org/10.1061/(ASCE)0733-9445(1997)123:9(1163).
19. Bogdan, T., Gerardy, J.C., Davies, D.W. and Popa, N., "Performance and capacity of composite "mega columns" with encased hot rolled steel sections", ***Euro Steel***, Vol. 1, No. 2-3, (2017), 1879-1888 DOI: https://doi.org/10.1002/cepa.232.
20. Lelkes, A. and Gramblička, Š., "Theoretical and experimental studies on composite steel–concrete columns", ***Procedia Engineering***, Vol. 65, (2013), 405-410 DOI: https://doi.org/10.1016/j.proeng.2013.09.063.

21. Nematzadeh, M., Fazli, S. and Hajirasouliha, I., "Experimental study and calculation of laterally-prestressed confined concrete columns", ***Steel and Composite Structures***, Vol. 23, No. 5, (2017), 517-527 DOI: https://doi.org/10.12989/scs.2017.23.5.517.
22. ACI, "Standard practice for selecting proportions for normal, heavyweight, and mass concrete(aci 211.1-91), ACI manual of concrete practice, (1996), 1-38.
23. ASTM, "E8/e8m-2013, standard test methods for tension testing of metallic materials, ASTM International, West Conshohocken, USA, (2013).
24. Nematzadeh, M. and Ghadami, J., "Evaluation of interfacial shear stress in active steel tube-confined concrete columns", ***Computers and Concrete***, Vol. 20, No. 4, (2017), 469-481 DOI: https://doi.org/10.12989/cac.2017.20.4.469.
25. Haghinejada, A. and Nematzadeh, M., "Three-dimensional finite element analysis of compressive behavior of circular steel tube-confined concrete stub columns by new confinement relationships", ***Latin American Journal of Solids and Structures***, Vol. 13, No. 5, (2016), 916-944 DOI: https://doi.org/10.1590/1679-78252631
26. ACI, "Building code requirements for structural concrete (aci 318-11), Detroit, MI, USA, (2011).
27. Barr, B. and Lee, M., "Modelling the strain-softening behaviour of plain concrete using a double-exponential model", ***Magazine of Concrete Research***, Vol. 55, No. 4, (2003), 343-353 DOI: https://doi.org/10.1680/macr.2003.55.4.343.
28. Zhao, X.-L., Han, L.-H. and Lu, H., "Concrete-filled tubular members and connections, CRC Press, (2010).

Persian Abstract

چکیده

ستون های بتنی مسلح شده با فولاد SRC نوعی از ستون های مرکب می باشند که به دلیل مزایای فراوانی که نسبت به ستون های بتن آرمه و فولادی تنها دارند، استفاده از آنها در سال های اخیر رواج زیادی پیدا کرده است. در این تحقیق، به جهت بررسی رفتار ستون های SRC، شاخص شکل پذیری این ستون ها و عوامل موثر بر آن مورد بررسی قرار گرفته و همچنین با محاسبه معادلات لازم بر اساس روش توزیع تنش پلاستیک، روشی ساده برای طراحی این ستون ها ارائه گردید. بر همین اساس، یک تست آزمایشگاهی بر روی 6 نمونه ستون SRC با دو نوع پروفیل فولادی H و صلیبی و با سه نسبت برون محوری 0.4، 0.55 و 0.7 انجام شد. همچنین یک مدل المان محدود به کمک نرم افزار آباکوس به جهت مطالعه عددی ایجاد شد که با نتایج مدل آزمایشگاهی اعتبارسنجی گردید. در مجموع 30 ستون برای مطالعه پارامتریک تحلیل گردیدند که متغیرهای هندسی و مصالح از قبیل درصد فولاد، مقاومت فشاری بتن، فاصله میلگردهای عرضی و شکل هندسی هسته فولادی بر شاخص شکل پذیری این ستون ها مورد بررسی قرار گرفتند که نتایج نشان داد که برای ستون با مقطع فولادی مانندH، کاهش نسبت فاصله آرماتورهای عرضی از 0.6 به 0.2 سبب افزایش شاخص شکل پذیری به میزان 72% می گردد که این کاهش فاصله، سبب ایجاد سخت شدگی پس از نقطه تسلیم در نمودار نیرو- تغییرمکان و افزایش ظرفیت باربری به میزان 20% نیز می گردد. همچنین بر اساس روش توزیع تنش پلاستیک ذکر شده در آیین نامه EC4، نمودارهای اندرکنش نیرو- لنگرخمشی ترسیم شده و با نمودارهای اندرکنش استخراج شده توسط نرم افزار مقایسه گردیدند و در نهایت نمودارهایی بدون بعد جهت طراحی این ستون ها ارائه شد.